Cell clusters adopt a collective amoeboid mode of migration in confined nonadhesive environments

Diane-Laure Pagès, Emmanuel Dornier, Jean de Seze, Emilie Gontran, Ananyo Maitra, Aurore Maciejewski, Li Wang, Rui Luan, Jérôme Cartry, Charlotte Canet-Jourdan, et al.

CANCER

Cell clusters adopt a collective amoeboid mode of migration in confined nonadhesive environments

Diane-Laure Pagès[1,2]†, Emmanuel Dornier[1]*†, Jean de Seze[3], Emilie Gontran[1], Ananyo Maitra[4]‡, Aurore Maciejewski[1,2], Li Wang[5], Rui Luan[1], Jérôme Cartry[1], Charlotte Canet-Jourdan[1,2]§, Joël Raingeaud[1], Grégoire Lemahieu[1]||, Marceline Lebel[1], Michel Ducreux[1,6], Maximiliano Gelli[1,7], Jean-Yves Scoazec[8,9], Mathieu Coppey[3], Raphaël Voituriez[4,10], Matthieu Piel[5], Fanny Jaulin[1]*

Cell migration is essential to living organisms and deregulated in cancer. Single cell's migration ranges from traction-dependent mesenchymal motility to contractility-driven propulsive amoeboid locomotion, but collective cell migration has only been described as a focal adhesion–dependent and traction-dependent process. Here, we show that cancer cell clusters, from patients and cell lines, migrate without focal adhesions when confined into nonadhesive microfabricated channels. Clusters coordinate and behave like giant super cells, mobilizing their actomyosin contractility at the rear to power their migration. This polarized cortex does not sustain persistent retrograde flows, of cells or actin, like in the other modes of migration but rather harnesses fluctuating cell deformations, or jiggling. Theoretical physical modeling shows this is sufficient to create a gradient of friction forces and trigger directed cluster motion. This collective amoeboid mode of migration could foster metastatic spread by enabling cells to cross a wide spectrum of environments.

INTRODUCTION

Emerging in early eukaryotes, migration is a fundamental property of cells that supports individual cell displacements and metazoan development and homeostasis (*1*). It is also deregulated in diseases, such as cancer, where it fuels their metastatic spread (*2*). Under normal and pathological conditions, cells enable three main modes of migration, based on their ability to move independently or collectively and the mechanism of force generation. Two distinct mechanisms are used by single cells to generate migration forces (*3*). They result from the cells' ability to interact with the surrounding extracellular matrix (ECM) and their level of contractility. In traction-based mesenchymal migration, integrin engagement with the ECM through focal adhesion converts branched-actin polymerization into large protrusions and forward forces (*3*, *4*). In contrast, amoeboid single cells use a propulsive locomotion that does not require specific adhesion and is driven by friction forces resulting from actomyosin retrograde flows (*5*, *6*). Cells can also move in a cohesive manner as a group, using the only mode of collective migration described so far, that is mechanistically equivalent to single cells' traction-based migration (*7*–*9*). At the front of the cluster, leader cells use the substrate as an anchor to pull on follower cells, instructing directionality and generating important traction forces via polarized actin-based protrusions. At the back, the higher contractility of the follower cells can generate the intercalation of rear cells and intracluster cellular flows to power collective chemotaxis (*10*–*12*). To date, our knowledge on collective cell movement suggests that it only takes the form of an adhesion-dependent traction-based mode of locomotion and the question as to whether it occurs through an alternative mechanism has never been raised.

RESULTS

Cancer cell clusters migrate in confined nonadhesive environments

The analysis of primary tumor explants harvested from patients with metastatic colorectal cancers (CRCs) identified TSIPs (tumor spheres with inverted polarity) (*13*). These tumor cell clusters have an inverted apico-basolateral polarity exposing the apical membranes to the microenvironment and precluding adhesion receptors from interacting with the surrounding ECM (Fig. 1, A and B). However, TSIPs efficiently invade surrounding tissues and are associated with high metastatic burden and poor patient prognosis (*13*). Moreover, in the course of their dissemination, cell clusters from other cancers encounter environments lacking ECM, such as the lumen of lymphatic vessels, in which they progress without the contribution of classical adhesion formation (also named lymphatic microemboli; Fig. 1C). These observations made from live and fixed primary tumor specimens raised the possibility of a focal adhesion–independent mode of collective cell migration.

To test this hypothesis, we engineered microchannels devoid of any physiological substrates or chemotactic cues but coated with the anti-adhesive polymer polyethylene glycol (PEG; Fig. 1D and fig. S1, A to C). Time-lapse imaging during 20 to 24 hours showed that

[1]Inserm U-1279, Gustave Roussy, Villejuif F-94805, France. [2]Université Paris-Saclay, Inserm, Institut Gustave Roussy, Dynamique des Cellules Tumorales, Villejuif 94800, France. [3]Laboratoire Physico Chimie Curie, Institut Curie, PSL Research University, Sorbonne Université, CNRS, Paris 75005, France. [4]Laboratoire Jean Perrin, UMR 8237 CNRS/Sorbonne Université, Paris 75255, France. [5]Institut Curie and Institut Pierre Gilles de Gennes, PSL Research University, CNRS, UMR 144, Paris 75005, France. [6]Département de Médecine Oncologique, Gustave Roussy, Université Paris-Saclay, Villejuif F-94805, France. [7]Département de Chirurgie Viscérale, Gustave Roussy, Villejuif F-94805, France. [8]Service de Pathologie, Département de Biologie et Pathologie Médicale, Gustave Roussy, Villejuif F-94805, France. [9]Faculté de Médecine, Université Paris Saclay, Le Kremlin-Bicêtre F-94270, France. [10]Laboratoire de Physique Théorique de la Matière Condensée, UMR 7600 CNRS/Sorbonne Université, Paris 75255, France.
*Corresponding author. Email: fanny.jaulin@gustaveroussy.fr (F.J.); emmanuel.dornier@gustaveroussy.fr (E.D.)
†These authors contributed equally to this work.
‡Present address: Laboratoire de Physique Théorique et Modélisation, CNRS UMR 8089, CY Cergy Paris Université, Cergy-Pontoise F-95302, France.
§Present address: Institut Curie, PSL Research University, INSERM U932, Paris F-75005, France.
||Present address: Department of Cellular Biophysics, Max Planck Institute for Medical Research, Heidelberg 69120, Germany.

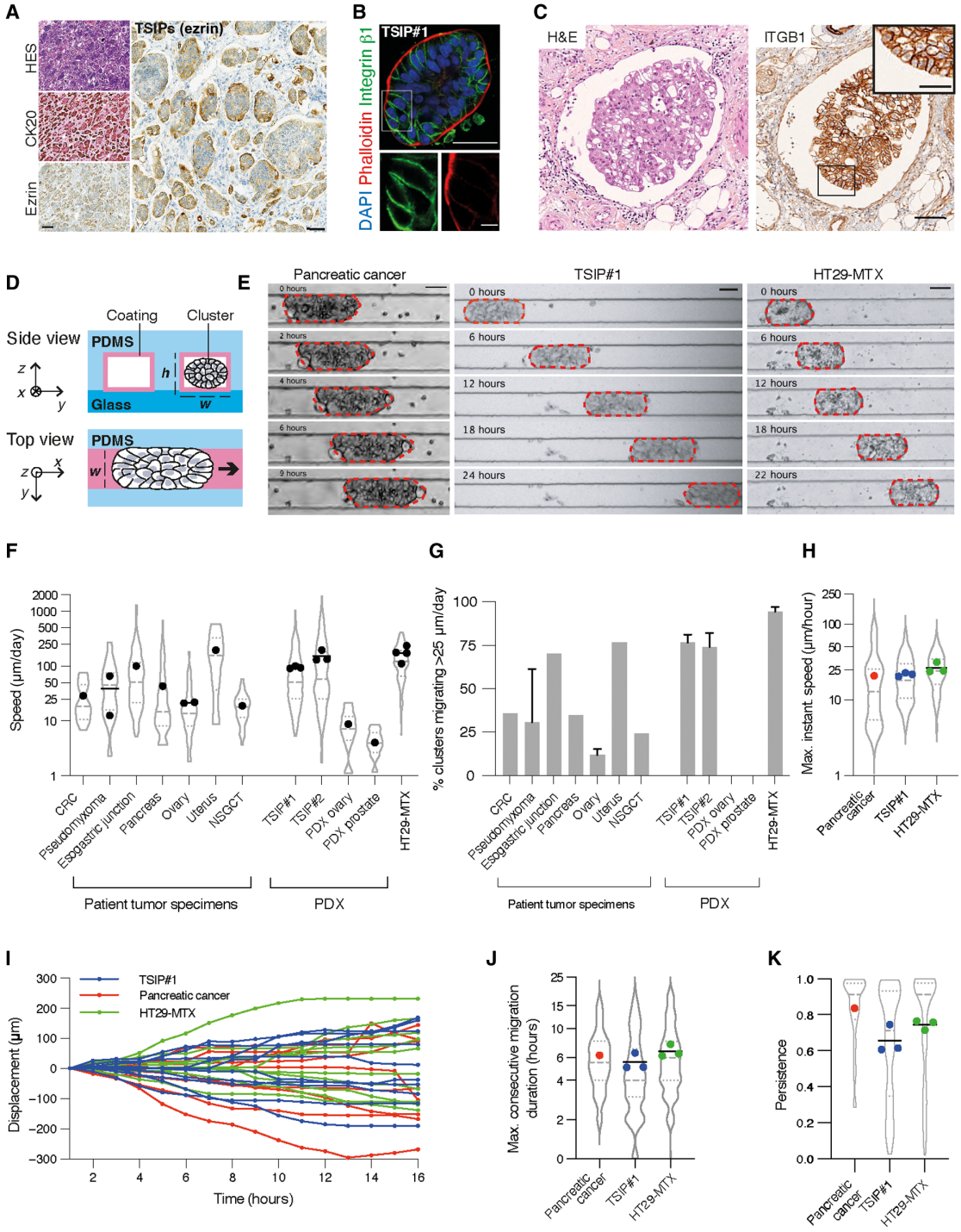

Fig. 1. Cell clusters from patient explants migrate in confined nonadhesive environments. (**A**) TSIPs (tumor spheres with inverted polarity) from a representative CRC tumor specimen (micropapillary). Low and high magnification. HES, hematoxylin/eosin/saffron; CK20, anti-cytokeratin 20. (**B**) Immunofluorescence of TSIP#1 after 24 hours in collagen I. The boxed region is shown at high magnification. (**C**) Tumor microemboli from CRC (mucinous). H&E, hematoxylin/eosin; ITGB1, anti-integrin β1. The boxed region is shown at high magnification. (**D**) Scheme, not to scale, of microchannels (width, $w = 60$ μm; height, $h = 30$ μm). (**E**) Time-lapse sequences of clusters migration from pancreatic cancer, TSIP#1, and HT29-MTX. (**F**) Mean migration speed of tumor clusters from patients and patient-derived xenografts (PDXs). CRC, colorectal cancer; NSGCT, nonseminomatous germ cell tumor. Log_{10} scale. Dots, mean speed over clusters for each independent experiment; lines, means over experiments. (**G**) Proportion of migrating (>25 μm/day) clusters. Error bars: SEM. For (F) and (G), $n = 14$ to 153 clusters per cell type. (**H**) Maximum instantaneous (Max. instant.) speed of clusters, log_{10} scale. (**I**) Representative tracks of clusters migrating in one direction (>0) or the other (<0). $n = 9$ to 10 clusters per cell type. (**J** and **K**) For clusters migrating substantially (>25 μm/day), duration of the longest period of consecutive migration (J) and persistence (K). $n = 38$ to 107 clusters. For (E) to (K), clusters migrate 1 day in PEG-coated microchannels. (F, H, J, and K) Dots, mean speed over clusters for each independent experiment; lines, means over experiments. Scale bars, 200 μm [(A), low magnification], 100 μm [(C), low magnification], 50 μm [(A) and (C), high magnification; (B), low magnification; (E)], and 10 μm [(B), high magnification].

TSIPs and primary explants from a variety of digestive and genitourinary cancers migrated into nonadhesive microchannels, some reaching up to 2 mm/day (Fig. 1, E to G, and movies S1 and S2). This migratory behavior was also recapitulated by clusters made from cell lines from several types of cancers, including circulating tumor cells (fig. S1, D to E). We further analyzed the migration of cell clusters from pancreatic (patient ascites) or CRC [TSIPs from patient-derived xenograft (PDX) or HT29-MTX cell line]. This analysis revealed that, on average, they migrated consecutively for about 6 hours (up to 19 hours), with a persistence of 0.66 ± 0.04 and 0.75 ± 0.01 for TSIP#1 and HT29-MTX, respectively (means ± SEM) and reached a maximum speed of 21.7 ± 0.7 μm/hour (TSIP#1) and 26.5 ± 2.5 μm/hour (HT29-MTX) (Fig. 1, H to K). Average speeds were 174 ± 25 μm/day for HT29-MTX and 95 ± 3 μm/day for TSIPs. Although quite slow when compared to single-cell migration in experimental settings, this speed is in the order of magnitude of collective migration speeds reported in vivo (*14*, *15*). Together, these experiments show that a variety of cancer cell clusters display a persistent motility when confined in nonadhesive environments.

Focal adhesion and traction forces are not required for cluster migration

Because HT29-MTX is the fastest and the easiest system for transgene expression, they were further used for the mechanistic studies. Migration in PEG-coated microchannels is associated with a compact rounded morphology that contrasts with the loose and spread shape observed when microchannels are coated with collagen I (Fig. 2A). Measuring the contact angles between the cluster boundaries and the microchannel walls highlighted the "dewetting" morphology of the clusters and the absence of protrusions for HT29, HT29-MTX, and TSIPs migrating in PEG-coated microchannels, as opposed to the "wetting" morphology of HT29 under collagen-coated conditions (Fig. 2, A and B). To address the contribution of focal adhesions to cluster migration, we expressed Turquoise- or mCherry-tagged paxillin in HT29-MTX. While fluorescent paxillin revealed numerous foci at the collagen-I interface, they were nearly absent in PEG-coated microchannels (Fig. 2, C and D, and movie S3). In addition, the collagen-I coating reduced HT29-MTX migration speeds (from 264.6 ± 14.95 to 92.76 ± 15.89 μm/day; Fig. 2E), in line with observations made from single cells where focal adhesion–dependent migration is slower than amoeboid migration (*6*). To assess the participation of focal adhesions, we inhibited two of their main regulators, focal adhesion kinase and Src, using different pharmacological inhibitors (PF271 and SU6656, respectively, or saracatinib). These treatments did not slow down the migration of HT29-MTX clusters in nonadhesive microchannels (Fig. 2F and fig. S2A). However, they inhibited focal adhesion formation in collagen-I–coated microchannels and could even rescue migration under these conditions (Fig. 2G and fig. S2, B to D). In line with this, measuring bead displacements in traction force microscopy experiments revealed that clusters exert no traction forces on PEG-coated polydimethylsiloxane (PDMS) substrates, as opposed to localized pulling forces observed on collagen-I–coated PDMS substrates (Fig. 2, H to I, and fig. S3). While integrins are essential components of focal adhesions, they also have alternative functions by transmitting propelling friction forces against the substrate during single-cell amoeboid migration (*5*, *16*). Inducing integrin internalization with a cyclic RGD peptide (cilengitide, cRGD) or a small-molecule inhibitor (SB273005) decreased migration speed in PEG-coated channels by 1.8- and 3.2-fold, respectively (Fig. 2J and fig. S2, E and F). To the contrary, increasing nonspecific friction forces using bovine serum albumin (BSA) speeded up migration by up to 56% and even partially rescued the migration of clusters treated with cRGD peptides (Fig. 2, K and L, and fig. S2G). Thus, these results indicate that, unlike traction-based collective migration (*8*, *10*, *12*), clusters rely on integrin-mediated friction forces to migrate without focal adhesions in nonadhesive microchannels.

Cluster migration relies on RhoA activation and polarized actomyosin contractility

We then reasoned that the actomyosin cytoskeleton could power this collective mode of migration (*5*, *6*, *17*, *18*). Expressing the fluorescent probe F-tractin and Turquoise-tagged myosin light chain (MLC) in HT29-MTX revealed a robust supracellular peripheral actomyosin cortex in median sections (Fig. 3A). Such structures were also observed in primary tumor explants and resemble the cytoskeletal organization described for other epithelial cells groups (fig. S1F) (*12*, *19*–*21*). The MLC cortex was evenly distributed in static clusters but displayed a strong polarization, with a twofold enrichment toward the back, during their migration (Fig. 3, A and B, and movie S4). Cluster front/back polarity was positively correlated with migration speed, suggestive of a pro-migratory function (Fig. 3C). This was confirmed by pharmacological inhibition of myosin II (blebbistatin) or Rho-associated protein kinase (ROCK) (Y27632) activities, which significantly reduced TSIP#1 and HT29-MTX migration speeds by 1.7- to 3-fold, respectively (Fig. 3, D to F). We then tested whether increasing contractility at the rear of the cluster was sufficient to power their migration. To this end, we used optogenetics to manipulate actomyosin contractility via its upstream regulator RhoA. We transduced HT29-MTX cells with either (i) the optoRhoA system that enables an acute spatiotemporal recruitment of RhoA activator ARHGEF11 to the membrane using the CRY2/CIBN light gated optogenetic dimerization system (Fig. 4A) (*22*) or (ii) the CRY2/CIBN optogenetic dimerizer without RhoA's activator as a control. We illuminated the front of migrating clusters and monitored their trajectories for up to 10 hours by using an automated stage and activation routine maintaining a constant illumination region despite the movement of the cluster (Fig. 4B). After illumination, 67% of optoRhoA clusters reverted their direction of migration, while only 13% of control clusters did (Fig. 4, C to E, and movies S5 and S6). Activation at the rear did not yield a significantly higher speed of migration, indicating that further increasing actomyosin contractility has no effect on cluster speed (Fig. 4E, green and black dots). This indicates that increasing actomyosin activity in a subset of cells dictates the direction, but not the speed, of migrating clusters. Together, these experiments show that the front/back polarization of the supracellular actomyosin cortex defines the direction of migration of the clusters.

Focal adhesion–independent collective migration occurs without persistent retrograde flows

Polarized contractility supports collective and single-cell migration by orienting the retrograde flows of cells or myosin (fig. S4) (*6*, *12*, *23*). We first investigated the participation of cell flows, described to power the collective migration of neural crest cell clusters or giant keratocytes aggregates (Fig. 5A, left) (*12*, *24*). To this end, we expressed red fluorescent protein (RFP)–tagged histone 2B (H2B) in HT29-MTX clusters and tracked individual cell movements during up to 11 hours of migration in nonadhesive microchannels. First,

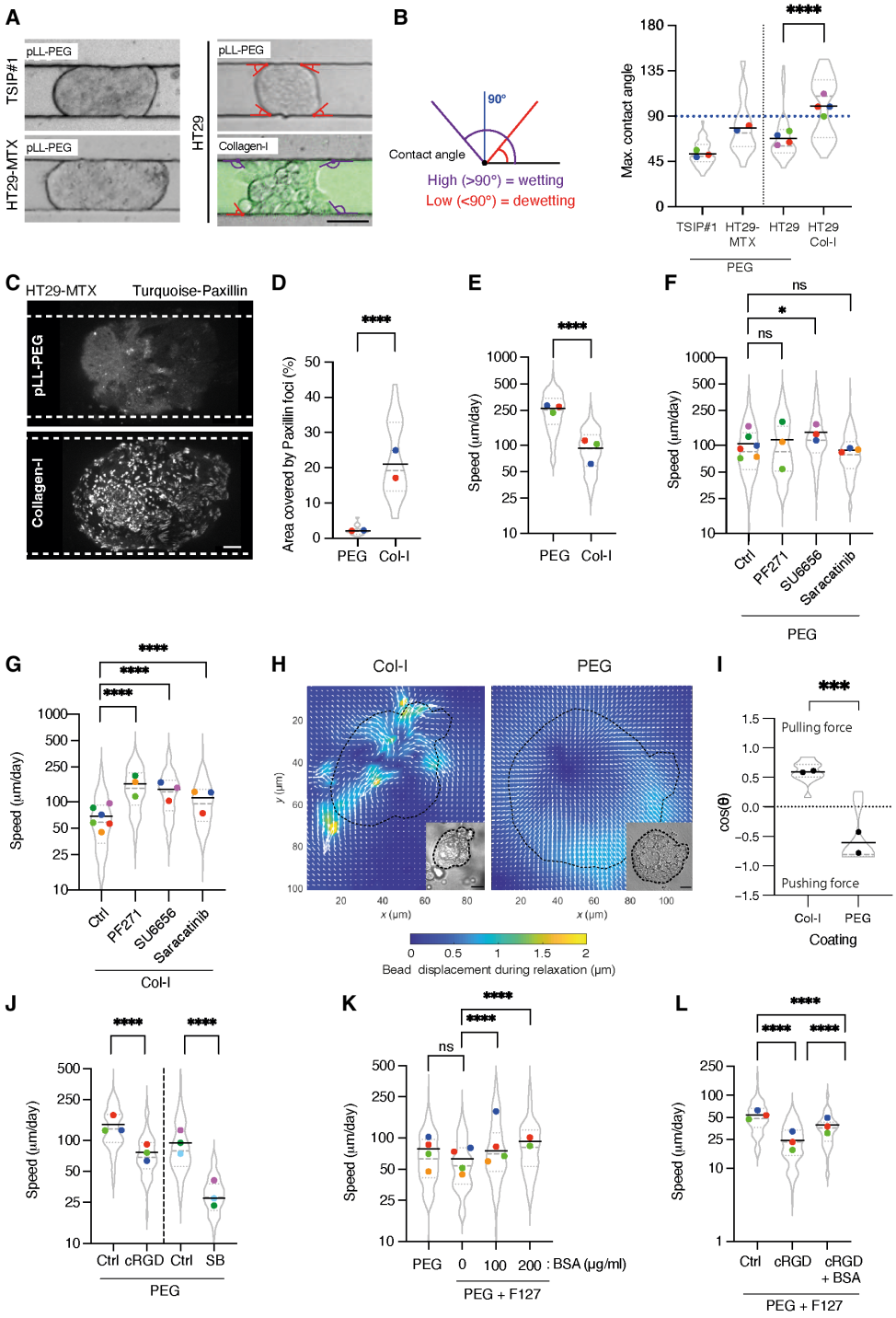

Fig. 2. Cluster migration in nonadhesive environments is traction independent but friction dependent. For (**A**) to (**G**), microchannels coating; PEG, pLL-PEG; Col-I, Cy5–collagen I. (A and B) Representative images (A; scale bar, 50 μm) and maximum (Max.) contact angle of clusters (B; $n = 39$ to 59, Mann-Whitney test). (C to E) Representative images of Paxillin at bottom planes (C; scale bar, 10 μm), area covered by Paxillin foci (D; $n = 19$ to 28), and mean speed of HT29-MTX clusters (E; $n = 90$ to 106) (Mann-Whitney tests). (F and G) Mean speed of HT29-MTX clusters treated in PEG-coated (F) or Col-I–coated (G) microchannels. PF271, PF562271. $n = 70$ to 182 (one-way ANOVA). (**H** and **I**) PIV maps of TFM measurements (bead displacements following SDS-mediated relaxation) (H; scale bars, 20 μm) and orientation of forces exerted by HT29-MTX clusters (I; $n = 8$ to 14, Welch's t test) on Col-I– or PEG-coated substrates. θ, angle between cluster radius and bead displacement vector (fig. S3B). On PEG, small pushing forces are probably due to agarose pad confinement. (**J**) Mean speed of HT29-MTX clusters. cRGD, cyclic RGD; SB, SB273005. $n = 74$ to 149 (Student's t tests). (**K**) Mean speed of HT29-MTX clusters. Microchannels coating: PEG ± F127 and BSA at indicated concentrations. $n = 78$ to 151 (one-way ANOVA). (**L**) Mean speed of HT29-MTX clusters treated with cRGD. Microchannels coating: PEG + F127 ± BSA (300 μg/ml; cRGD + BSA). $n = 67$ to 82 (one-way ANOVA). n, number of clusters; ns, not significant; $^*P < 0.05$, $^{***}P < 0.001$, and $^{****}P < 0.0001$. For each panel, SuperPlots, violin plot (all clusters); dots, mean of each experiment; same color, same independent experiment; black line, mean of individual means (see the "Data presentation, statistics, and reproducibility" section).

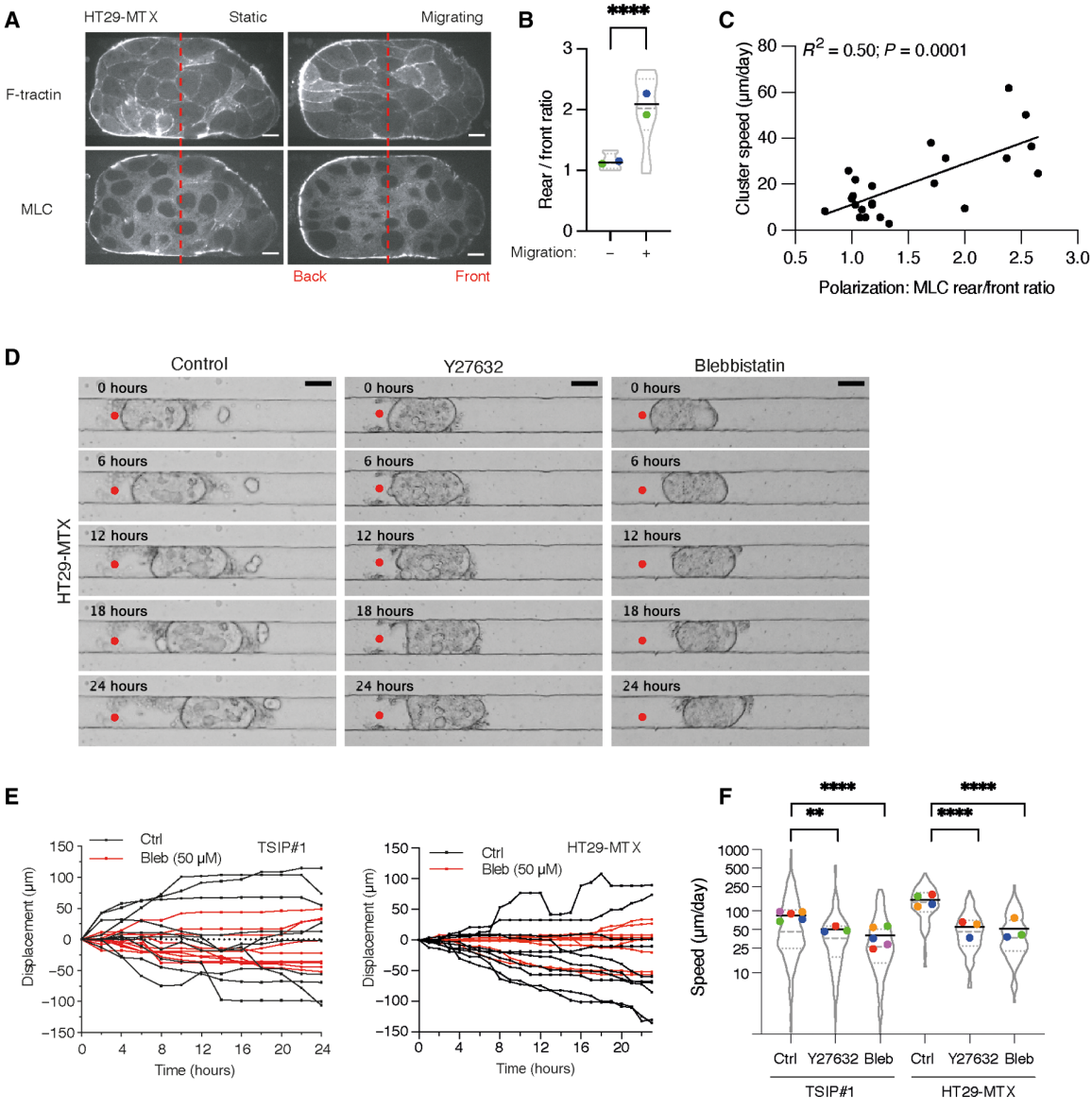

Fig. 3. Focal adhesion–independent collective migration is driven by the contractility of the polarized actomyosin cortex. (**A**) Median section of HT29-MTX stably expressing F-tractin–mRuby3 (top) and mTurquoise-MLC (bottom), in PEG-coated channels. Red dashed lines visually materialize the front and back of clusters for quantification of ratio in (**B**). Scale bars, 10 µm. (B) Polarization of clusters expressed as MLC expression ratio between rear and front of clusters migrating in PEG-coated or PEG + F127–coated microchannels, as indicated in Materials and Methods. $n = 12$ to 13 clusters. (**C**) Correlation between cluster speed and polarization of clusters; statistics for linear regression are shown on the graph. $n = 23$ clusters from three independent experiments. (**D**) Time-lapse sequences of HT29-MTX clusters migrating in PEG-coated microchannels in control condition and under Y27632 (25 µM) or blebbistatin (Bleb; 50 µM) treatments. Red dots, starting position of the clusters. Scale bars, 50 µm. (**E**) Representative tracks of clusters treated with Bleb or with DMSO (Ctrl). $n = 10$ clusters for each cell type. (**F**) Mean speed of clusters treated with Y27632, Bleb, or DMSO (Ctrl); $\log_{10}$ scale. $n = 106$ to 205 clusters (one-way ANOVA). $^{**}P < 0.01$ and $^{****}P < 0.0001$.

we did not identify notable exchange between neighboring cells (Fig. 5, B to D, and movie S7). In addition, the averaged velocity of individual cells, in particular cells in contact with the channel walls, was anterograde (Fig. 5, D and E, and movie S7). Thus, the clusters move cohesively as solids in absence of sustained retrograde cellular flows, excluding cell treadmilling as the main migration mechanism (Fig. 5A, right). We next evaluated whether propulsive forces could be generated at the subcellular scale by actomyosin retrograde flows using Turquoise-MLC [its signal appeared more granular than actin, which helps for particle image velocimetry (PIV) analysis, and provided more signal-to-noise ratio]. PIV confirmed that HT29-MTX migrating as single cells displayed persistent and coordinated myosin retrograde flows, as described during amoeboid migration (fig. S4 and movie S8) (*6*, *18*, *23*). In clusters, PIV analyses were performed over long periods of time (scale of hours), on the cluster contact areas with the substrate from median planes (Fig. 5, F to H). When averaged over time and multiple clusters, these PIV analyses yielded mostly anterograde flows in the substrate frame of reference (Fig. 5, F to H, and movie S9). This therefore excludes the contribution of persistent actomyosin retrograde flows at the single-cell

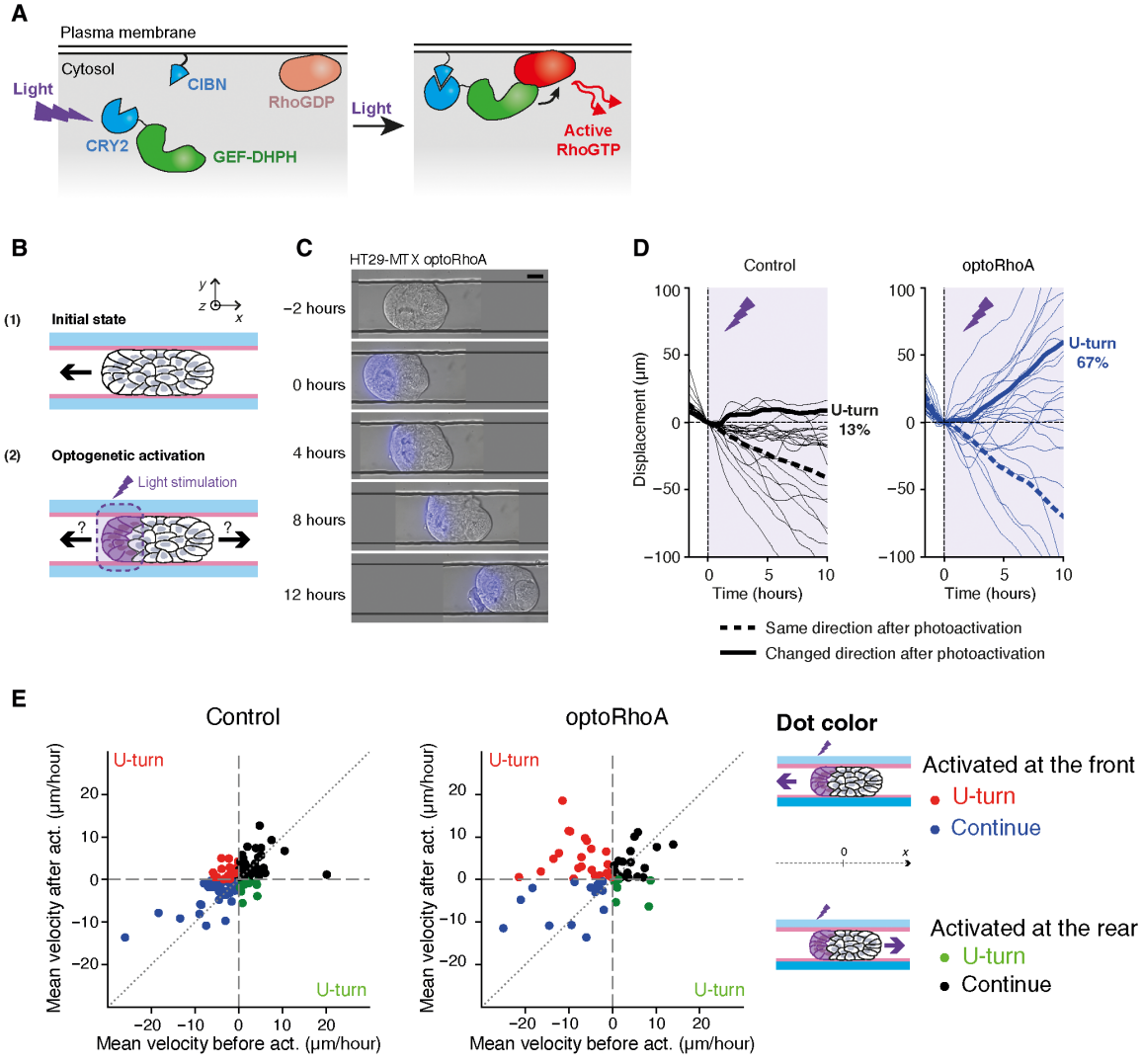

Fig. 4. Polarized RhoA activation dictates the direction of migration. (**A**) Schematic of the molecular effect of light activation in optoRhoA cells. (**B** and **C**) Optogenetic manipulations: experimental setup (B) and representative time-lapse sequence (C). Scale bar, 20 µm. (**D**) Displacement of clusters over time before (−1 hour 30 min < t < 0 hours) and after (0 hours < t < 10 hours) optogenetic activation of control and optoRhoA–stably expressing HT29-MTX cells. Bold lines are the mean displacement of clusters changing direction (mean displacement after activation, >0). Dotted lines are the mean of clusters not changing direction (mean displacement after activation, <0). Purple zone, optogenetic activation. n = 23 for control and n = 24 for optoRhoA from at least three independent experiments. P = 0.0003 (Fisher's exact test on the proportion of turning clusters). (**E**) Left: Mean velocity before (average over 1 hour 30 min, x axis) and after (average over 10 hours, y axis) activation (act.) of control and optoRhoA clusters. n = 119 (control) and 62 (optoRhoA) clusters. Right: Schematic of activation protocol, showing corresponding colors on the graph shown on the left panel.

level, coordinated at the cluster scale, as the propulsive mechanism. Together, tracking cells and their actomyosin cytoskeleton showed that migrating clusters translate as a whole and do not use any of the known mechanisms of cell migration, which are based on sustained retrograde flows, either at the cellular or intracellular levels (*1*, *7*).

Cluster migration is associated with fluctuating cell deformations or "jiggling"

Thus, we investigated alternative mechanisms. Single cell confined into microchannels can be powered by an "osmotic engine" based on the asymmetrical distribution of Na^+/H^+ pumps (*25*). We inhibited these pumps using 5-(*N*-ethyl-*N*-isopropyl)amiloride (EIPA) treatment but did not observe any effect on cluster migration speeds (fig. S5A). Therefore, the osmotic engine mechanism would require an osmolarity gradient between the front and rear of the cell and thus would rely on the fact that there is no space for diffusion between the cell and the channel walls. We designed microchambers where clusters are only confined top to bottom but not on the sides. While fluids could freely flow around the clusters, they migrated very efficiently in the chambers (even faster than in channels), further proving that osmotic gradients and fluid fluxes are not at play (fig. S5B).

We then used a higher time resolution, in the order of minutes, to resolve the transient actomyosin dynamics using Turquoise-MLC. PIV analyses identified complex myosin flow patterns in the lab reference frame. In contact with the substrate, myosin flow velocities displayed fluctuations in amplitude over time, with stochastic and short-lived retrograde flows indicative of transient propulsive events (Fig. 6A and fig. S6A). PIV analysis of myosin flows

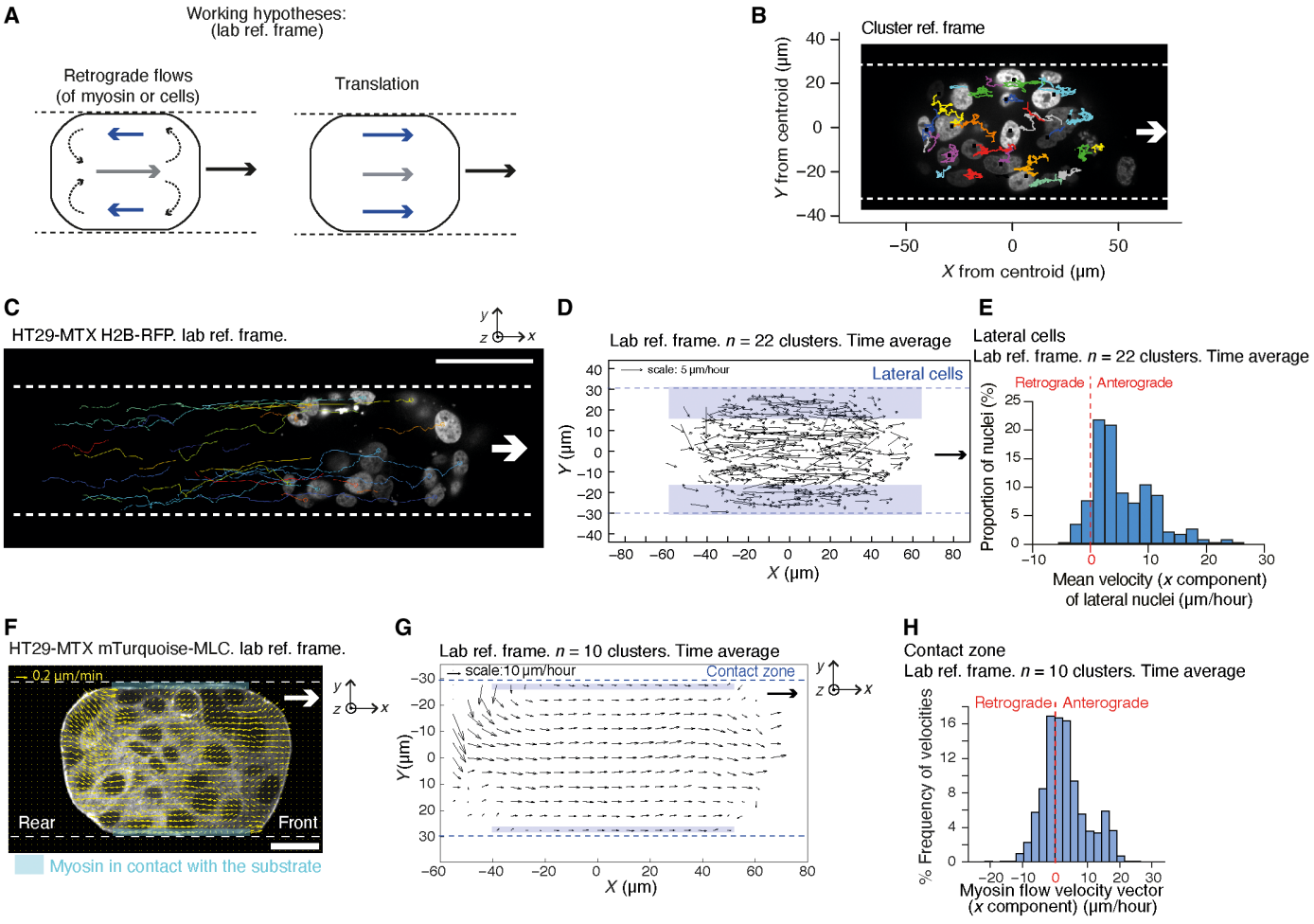

Fig. 5. Focal adhesion–independent collective migration occurs without persistent retrograde flows. (**A**) Schematic representation of cell treadmilling (left) and translation of the whole cluster (right). (**B**) Representative tracks of nuclei in the cluster reference frame. Median section of a histone 2B (H2B)-RFP–expressing HT29-MTX cluster, migrating to the right in a PEG-coated microchannel over 11 hours. The image is the first time point. (**C**) Representative example of nuclei tracks in the lab reference frame. Median section of an H2B-RFP–expressing HT29-MTX cluster, migrating in a PEG-coated microchannel over 10 hours. Scale bar, 50 µm. (**D**) Superimposition of the maps of individual nuclei displacements for $n = 22$ clusters (from seven independent experiments). Nuclei are tracked in median sections of H2B-RFP–expressing HT29-MTX clusters migrating in PEG-coated microchannels (25 min to 11 hours). Blue boxes, lateral nuclei defined for further nuclei speeds analysis (15 µm thickness at the contact with the channel walls). (**E**) Frequency distribution of the *x* component of the mean velocity of every lateral nucleus. Same clusters as in (D). (**F**) Median section showing instantaneous myosin flow velocity vectors superimposed on the raw image and detected by particle image velocimetry (PIV) of a representative HT29-MTX cluster–expressing mTurquoise-MLC and migrating in a PEG-coated channel. Time point, $T = 58$ min. Blue boxes, contact zone defined for further myosin flows analysis (2 µm thickness at the contact with the channel walls). (**G**) PIV map of myosin flow velocity vectors of median sections of clusters, averaged over time (25 min to 7.4 hours) and clusters ($n = 10$ migrating clusters from four independent experiments). (**H**) Frequency of velocities (*x* component) of myosin flow velocity vectors at the contact obtained from PIV maps of median sections. Same clusters as in (G).

at the bottom planes of clusters showed similar results (fig. S6, C and D). Because it is still experimentally challenging to measure forces associated with the retrograde/propulsive events, we used the amplitude of myosin flow or nuclei speed fluctuations at the contact with the channels walls as a proxy. To quantify them, their velocities in the cluster reference frame were centered around zero, i.e., their algebraic temporal mean was subtracted. We found that fluctuations of myosin flows at the cortex closely correlated with fluctuations of nuclei displacements observed in lateral cells (first layer in contact with the substrate) but also throughout the cluster, with more movement in fast moving clusters (Fig. 6, B and C, and fig. S6B). The amplitude of these fluctuations, or jiggling, was positively correlated with cluster migration speed: The more myosin/nuclei speeds fluctuate, the faster the cluster (Fig. 6, B and D, and fig. S6, E and F, on movies with either short or long time intervals). The amplitude of fluctuations was only correlated to movement in clusters migrating more than 2 µm/hour, indicating that jiggling is not by itself sufficient to drive migration (Fig. 6D and fig. S6, E and F). Polarization of the actomyosin cortex not only correlated with migration speed (as shown in Fig. 3, A to C, and fig. S6G) but also strongly correlated with persistence (Fig. 6E and fig. S6G). Together, these results suggest that polarization could harness jiggling to power persistent, directed migration. We then used theoretical physical modeling to determine whether these two minimal components are sufficient to power cluster migration.

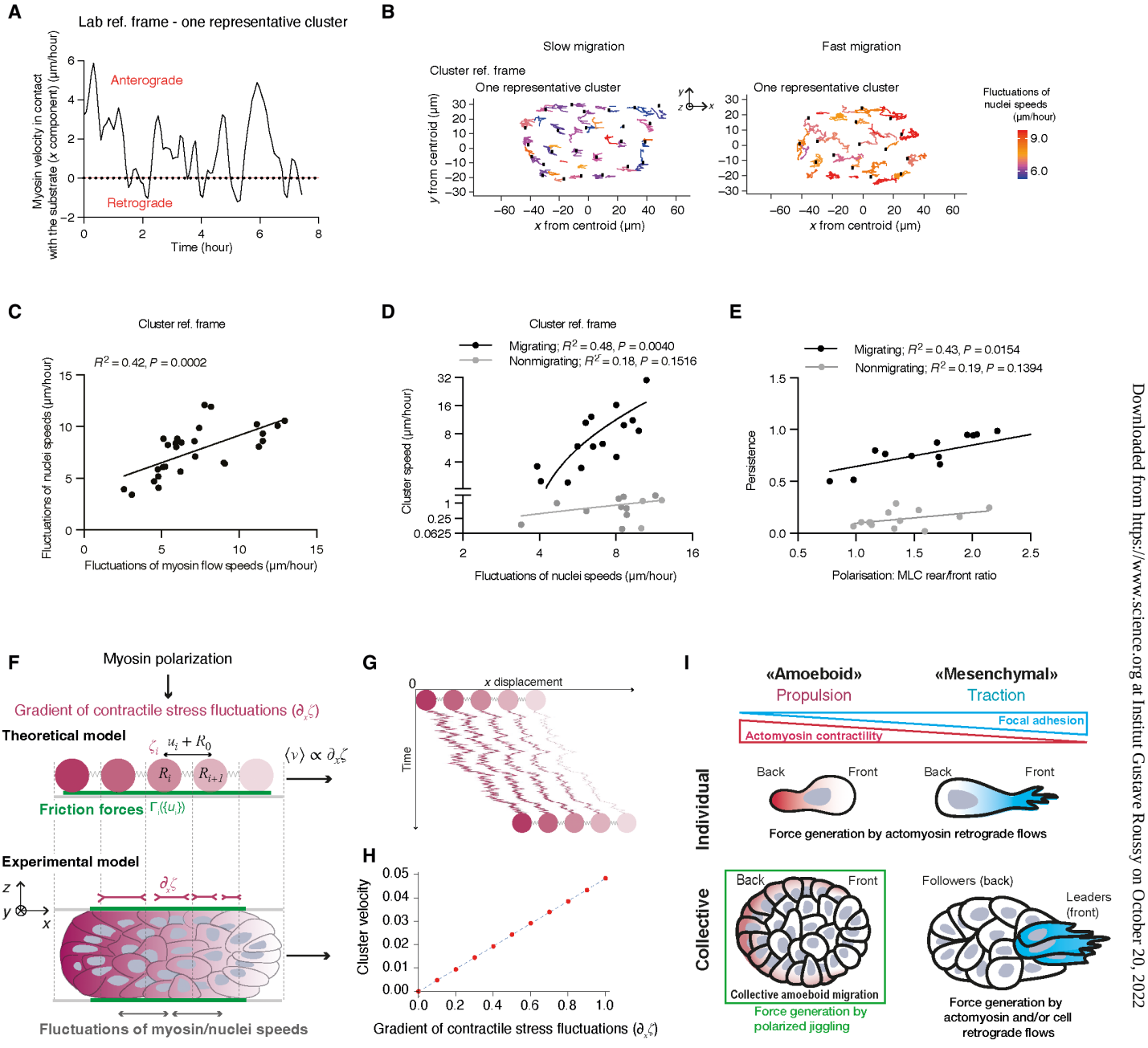

Fig. 6. Cell deformations and actomyosin polarity are the minimal components for collective amoeboid migration. For (**A**), (**C**), and (**D**), myosin and nuclei are analyzed at the contact with channels walls (see Fig. 5, D and G, and Materials and Methods) in median sections of HT29-MTX clusters migrating in PEG-coated microchannels. (A) Representative kinetics of myosin flow velocity (*x* component, spatial average). Lab ref. frame. (**B**) Nuclei tracks in representative clusters, every 2 to 10 min over 8 to 11 hours. Cluster ref. frame. (C) Amplitudes of myosin flows and nuclei speeds fluctuations. (D) Amplitudes of nuclei speeds fluctuations and cluster speeds (i.e., centroid direct displacement between first and last time point over total time, as migrating clusters do not change direction). Log_2 scales. (**E**) Cluster migration persistence correlation with myosin (MLC) polarization. For (C) to (E), lines, linear regressions; threshold between migrating/nonmigrating clusters, 2 µm/hour. $n = 27$ to 28 clusters (six independent experiments). (**F**) Discrete, five-beads one-dimensional model of the cell cluster, averaged along the *z* direction and discretized along the *x* direction. R_0, average separation; gray springs, elastic elements; color gradient represents the gradient of active fluctuations of contractile stress (ζ_i and $\partial_x\zeta$); friction forces (Γ_i, green) depend on the local strain $u = R_{i+1} - R_i - R_0$; *v*, cluster velocity. (**G**) Representative trajectory obtained from a stochastic simulation of (F). Mobility $M_i = \Gamma_i^{-1} = M_0 + M_1 u_i$; elastic potential $\cdot_i k u_i^2/2$; distance, units of R_0; time, units of $1/M_0 k \equiv \Gamma_0/k$. (**H**) Numerical evaluation of mean cluster velocity and $\partial_x\zeta$ (see Supplementary Text and fig. S10). (**I**) Schematic representation of the four main different modes of cell migration.

Collective amoeboid migration could arise from polarized jiggling

Inspired by earlier analytic descriptions of synthetic crawling or swimming machines (*26*–*28*), we propose a minimal physical model for collective amoeboid migration that describes the cluster as an actively polarized jiggling elastic solid, migrating despite any persistent cellular or myosin flow (Supplementary Text). This mechanism stems from the observed polarization of the clusters (Fig. 3, A to C) and their migration speed being correlated with the amplitude of both myosin and nuclei flow fluctuations (Fig. 6D and fig. S6E). The cluster is endowed with a fluctuating contractile stress, whose magnitude ζ follows the local myosin concentration and therefore displays a front-back gradient $\nabla\zeta$, which, in turn, causes a gradient of fluctuating deformations (Fig. 6F). This is the key ingredient that drives the cluster out of equilibrium and is eventually responsible for self-propulsion (Fig. 6, F to H). Data presented in Fig. 2 suggest that clusters interact with the substrate via passive friction forces, which are generically nonlinear and assumed to be strain (i.e., deformation) dependent. We provide in Supplementary Text a proof-of-principle calculation showing that the presence of fluctuating movements of myosin flows and/or nuclei, the polarization of the actomyosin cortex, and the transmission of passive friction forces with the substrate are the minimum ingredients to induce cluster self-propulsion, with velocity $v \sim \nabla\zeta$, independently of any sustained retrograde flow of actomyosin or nuclei (Fig. 6, C to H). Thus, in this general migration mechanism that we named "polarized jigging," self-propulsion arises from a front-back asymmetry of friction forces with the substrate, which is induced by fluctuating deformations within the cluster under a polarized myosin cortex. This can be seen as a micrometer-scale, continuous, stochastic version of vibrating crawling robots whose motion is based on cycling asymmetric friction forces on a substrate (*29*–*31*).

DISCUSSION

Identified from patient explants, we report an undescribed mode of migration that we named "collective amoeboid" based on several key features shared with amoeboid single-cell motility (Fig. 6I): Like a giant super cell, clusters mobilize their polarized supracellular actomyosin cortex to generate propulsive friction forces and migrate in absence of focal adhesion–mediated traction. However, the mechanism producing motility is completely different: Neither cell nor actomyosin retrograde flows are coordinated at the cluster scale. This ruled out conventional models of migration such as cell treadmilling described by the Mayor lab (*12*) or other "toothpaste-like" models comparable to the bleb-based mode of migration of single cells (*1*, *6*, *18*). Instead, we identified random fluctuations of myosin flows and cell displacements in migrating clusters. Our experimental evidence are supported by our physical theoretical model validating a mechanism of polarized jiggling based on a polarized contractile stress that yields directed motion in nonadhesive environments. This mechanism is consistent with the migration of engineered biological robots made by Kriegman *et al.* (*32*). In this system, asymmetric biological aggregates made of noncontractile stem cells and contractile cardiomyocytes are able to generate directed motion without temporal coordination of the contractions. Our study proposes a mechanism that requires only minimal elements: a front-back polarization, the presence of random contractile forces at the cluster scale, and nonspecific friction forces with the environment. We anticipate that this principle underlying the migration of cancer cell clusters could be extended to understand the movement of other biological systems.

In the course of their metastatic dissemination, tumor cells hijack all modes of single or collective migration described to date (*33*). Here, we show that cancer primary specimens and cell lines can also adopt collective amoeboid migration. This can result from intrinsic oncogenic features, such as in TSIPs, where the inverted apicobasolateral polarity prevents cluster adhesion to ECM-rich tissues (*13*), but we have shown that this apical-out configuration is not a prerequisite to collective amoeboid migration (Fig. 1F). This propulsion-based mode of collective migration could also be enabled as a non–cell autonomous process, when cancer cell clusters are confined into environments that they are unable to adhere to. These encompass major dissemination routes that are deprived of conventional ECM, such as perimuscular tracks, the lumen of lymphatic vessels, or the peritoneal and pleural cavities (*33*–*39*). It could also endow the migration of cell clusters across a wide spectrum of tissues for which they may not express the correct repertoire of receptors, reminiscent of leukocytes navigating all kinds of environments using an integrin-independent mode of migration.

MATERIALS AND METHODS

Data presentation, statistics, and reproducibility

Data are presented using SuperPlots, which are a superposition of the whole data distribution displayed as a violin plot and the mean of each individual experiment displayed as dots (*40*). In the violin plots, the whole population of clusters is displayed with the median (dashed gray line) and quartiles (dotted gray lines). Except for Fig. 1 and fig. S1 (see corresponding legends), dots of the same color represent the mean of matched control and experimental conditions performed in each individual experiment (red control dot goes with the red experimental condition dots). The black line is the mean of all experiments for each condition. To display lognormal distributions using violin plots, we first log-transformed the raw data and plotted them on a linear axis. For ease of read, we annotated the *y* axis with the antilog values.

Normality or log normality of all data distribution was tested using the Kolmogorov-Smirnov, d'Agostino-Pearson, or Shapiro-Wilk test in Prism 9 (GraphPad). When distributions are best fitted by a log normal distribution, statistical tests were performed on log-transformed data. Significance for datasets displaying normal distributions was calculated in Prism with unpaired (unless otherwise specified) two-tailed Student's *t* test or one-way analysis of variance (ANOVA) and Dunnett's multiple comparison test when comparing more than two conditions. Significance for non-normally distributed datasets were calculated in Prism using a Mann-Whitney test or a Welch's *t* test for different SD, or a Kruskal-Wallis test and Dunn's multiple comparison test when comparing more than two conditions. *P* values of statistical significance are represented as $*P < 0.05$, $**P < 0.01$, $***P < 0.001$, and $****P < 0.0001$; ns, not significant. *n* numbers of clusters per cells analyzed are indicated in the figure legends. The number of independent experiments (biological and technical replicates) is either represented on SuperPlots as the number of dots, either indicated in the figure legend. Experiments were performed independently for each cell line.

Biological material and cell culture

Human primary specimens

The human study protocols followed all relevant ethical regulations in accordance with the Declaration of Helsinki principles. The study

was approved by the ethics committee of Gustave Roussy hospital, and written informed consent was obtained from all patients.

Recovery of peritoneal effusions from patients

Tumor cell clusters from patients with CRC (with a 50% mucinous contingent) and pseudomyxoma are harvested by collecting serous fluid after addition and reabsorption of 500 ml of saline solution immediately after laparotomy. Ascites from patients with esogastric, pancreatic, ovarian, and uterus cancer are collected at day hospital. The processing of peritoneal effusions is adapted from the protocol described in (*13*). Briefly, fresh specimens are centrifuged twice at 400*g* for 5 min, and tumor cells are isolated via a Ficoll-Paque PLUS (GE HealthCare, 17144002) centrifugation, following the manufacturer's protocol. Cell clusters are then purified from single cells through several pulse centrifugations at 400*g*.

The nonseminomatous germ cell tumor specimen was isolated from biopsy. Tumoroids are kept in Matrigel for 6 weeks in colon organoid medium (*41*). They are then gently resuspended with TrypLE 1× and kept in suspension in an ultralow adhesion six-well plate (Corning, CLS3471-24EA) overnight before use in the microchannels.

Tumoroids generated from PDXs

Two human colorectal tumors (TSIP#1 corresponding to LRB-0009C and TSIP#2 corresponding to IGR-0014P) from the CReMEC tumor collection (*42*) were maintained in immunocompromised NOD *scid* gamma (NSG) mice (males or females). Animal experiments are compliant with French legislation and EU Directive 2010/63. The project received a favorable evaluation from Animal Care and Use Committee no. 26 and granted French Government authorization under number 517-2015042114005883 and 8867-2017020914112908. Mice were obtained from Charles River and Gustave Roussy in-house facility, housed and bred at the Gustave Roussy animal core facility (accreditation D94-076-11), and euthanized following endpoints validated by the Ethical Committee and the French government (Ministère de l'Enseignement Supérieur, de la Recherche et de l'Innovation). Tumoroid (TSIP) formation from PDXs was adapted from the protocol described in (*13*). Tumors between 1000 and 1500 mm^3 are minced and incubated in 5 to 10 ml of Dulbecco's modified Eagle's medium (DMEM) containing GlutaMAX (Gibco, 31966-021) supplemented with collagenase VIII (2 mg/ml; Sigma-Aldrich, C2139) for 1 hour and 15 min at 37°C under agitation. Tumor fragments are resuspended in 50 ml of DMEM and filtered through 100-μm cell strainers (EASYstrainer, 542000). Filtered tumor cells and clusters are pelleted at 800*g* for 10 min. Pellets are further washed four times by adding 10 ml of DMEM medium and pulse-centrifuged at 800 and 400*g* to collect clusters only. Clusters are kept in suspension in ultralow adhesion six-well plates (Corning, CLS3471-24EA) with DMEM medium supplemented with 10% fetal bovine serum (FBS; Gibco, 10270-106) (hereafter referred to as "full DMEM"). They form tumoroids after 3 days of culture.

Prostate cancer PDX (MR191) and ovarian cancer PDX (MR0097) are gifts from C. Robert's lab. Tumor fragments were digested to form clusters after 2 and 7 days of culture in six-well ultralow attachment plates in prostate culture medium (*43*) and full DMEM, respectively. All media are supplemented with 1% penicillin and streptomycin (Gibco, 15140-122).

Cell lines

Triple-negative breast cancer SUM52PE cells (gift from F. André's lab) and LS513 cells [CRC; American Type Culture Collection (ATCC), CRL-2134] are cultured in RPMI (RPMI 1640 1×, Gibco, 61870-010) medium supplemented with 10% FBS. HT29 (ATCC HTB-38, CRC) cells from human colon adenocarcinoma are grown in full DMEM. Mucous-secreting HT29-MTX (clone E12; European Collection of Authenticated Cell Cultures, 12040401, CRC) cells, derived from HT29 cell line, are grown in full DMEM supplemented by 1% nonessential amino acids (Gibco, 11140050). HT29 and HT29-MTX cell lines are used for mechanistic studies because they are the fastest cell lines and can be easily infected to express tagged proteins or trackers. Cell lines are dissociated with 0.05% trypsin-EDTA for passaging. For cluster production, 1.5 million cells are plated in a petri dish (nonculture coated) with 10 ml of culture medium for 3 to 5 days.

Circulating tumor cell lines (CTC44 and CTC45) are from human CRC (gift from J. Pannequin's lab) and cultivated, as previously described (*44*). In brief, they are maintained in suspension as clusters in advanced DMEM-F12 (Gibco, 12634-010) supplemented with 1% GlutaMax (Invitrogen, 35050-061), 1% N_2 supplement (Invitrogen, 17502-048), human epidermal growth factor (20 ng/ml), and human fibroblast growth factor–2 (10 ng/ml). They are split once a week, by pelleting at 300*g* for 5 min and incubated with Accumax for 45 min at 37°C. Phosphate-buffered saline (PBS; 5 ml) containing 2% FBS is then added to inactivate Accumax. Clusters are filtered through a 40-μm strainer, pelleted, and resuspended in M12 medium. All cell lines and clusters are cultured in a humidified incubator at 37°C under a 5% CO_2 atmosphere.

Microchannels, drug incubation, and cluster loading

Design of the channels

We designed microchannels with the following dimensions: height, $h = 30$ μm; width, $w = 60$ μm; and length, $l = 7$ mm. For chambers, $w' = 500$ μm. The loading chamber's height is $h = 180$ μm. Each chip contains three independent series of 30 microchannels and is dimensioned to fit in a 25-mm-diameter well. Epoxy molds are made from an original mold fabricated on a silicon wafer by standard photolithography with an SU8 photoresist (Microchem), following the manufacturer's instructions.

Microchannel preparation and drug incubation

Chips are made of a PDMS mixture (Neyco, RTV615) 10:1 (w/w) ratio with cross-linker, poured on the epoxy mold, and polymerized at room temperature for at least 48 hours. Loading ports are made with a 1-mm hole puncher. Chips are sterilized with 70% ethanol for a few minutes, dried, and activated for 1 min in a plasma chamber (Diener, Zepto V2, 30 W), together with a glass substrate [12-well glass-bottom plate (CellVis, P12-1.5H-N) or 25-mm glass coverslip for optogenetic experiments]. The 12-well glass-bottom plate is previously plasma-activated alone for 5 min. PDMS chips are stuck to the activated glass and heated at 95°C for 30 s for maximum binding. They are then cooled at room temperature for a few seconds before coating for at least 30 min with an anti-adhesive reagent [pLL-g-PEG (0.1 mg/ml; pLL(20)-g[3.5]-PEG(2) from SuSoS) or pLL-g-PEG + 1% pluronic F-127] or rat-tail collagen I (20 μg/ml; Corning, 354236). For Fig. 2A, collagen I is labeled with Alexa Fluor 647 (coupling of the collagen was done in-house, using Invitrogen labeling kit no. A20006). For the experiments in Fig. 2, BSA was added at the indicated concentrations in the PEG + F127 mixture for coating the channels. This was previously shown to increase friction (*18*). Chips are washed once in full DMEM and then submerged with medium for 1 hour to overnight.

For drug treatments [Y27632 (25 μM; Sigma-Aldrich, Y0503-5MG), blebbistatin (50 μM; Calbiochem, 203391), cyclic RGD

(10 μM; cilengitide, Selleckchem), SB273005 (10 μM; Selleckchem), PF562271 (250 nM; TargetMol), saracatinib (100 nM; MedChem Express), SU6656 (10 μM; Sigma-Aldrich), EIPA (20 and 50 μM; Sigma-Aldrich), or dimethyl sulfoxide (DMSO)], chips are incubated with medium and drugs 1 to 5 hours before cluster loading.

Cluster loading

Clusters are filtered on a 70-μm strainer (EASYStrainer, 542070), pelleted by a 400*g* pulse centrifugation and resuspended at 250 clusters/μl in full DMEM. Clusters are loaded using a 25-μl syringe (Hamilton, 702SNR 22/51 mm/pst3). All media are supplemented with 1% penicillin and streptomycin.

Flushing of the channels

After 1 day of migration in PEG-coated or collagen-I–coated microchannels, HT29-MTX clusters are flushed very gently with a syringe filled with water, at 2.8 μl/min. The whole chips are imaged before and after flushing at ×4 magnification on an Olympus inverted X83 microscope with a Hamamatsu camera. Clusters before and after flushing are then counted to quantify the effect of flushing, as a proxy for adhesiveness of the microchannels.

Single-cell experiments

Microchannels have the following dimensions: $w = 20$ μm and $h = 3$ or 5 μm. They are stuck to a 12-well plate or to a μ-dish (ibidi, 81151) following the experimental procedure described above and are coated with pLL-PEG. Single cells in suspension are then pushed inside the channels using a 25-μl Hamilton syringe (Hamilton, 702SNR 22/51 mm/pst3).

TFM setup preparation

Protocol adapted from (*18*).

Soft PDMS substrate preparation

A 100-μm-thick soft PDMS layer is made of PDMS mixture (CY 52-276, A + B) 1:1 (w/w) ratio of A to B, spin-coated (spin acceleration of 250 rpm/s, 500 rpm during 10 s and then 750 rpm during 40 s) on a FluoroDish [35 mm; World Precision Instruments (WPI), FD35-100] and let to polymerize overnight at 80°C.

Soft PDMS substrate functionalization

Substrates are silanized using a 1:10 (v/v) solution of 3-aminopropyltriethoxysilane (Sigma-Aldrich, A3648) diluted in 100% lab-grade ethanol. Substrates are incubated for 10 min in the silane solution, rinsed three times with 100% ethanol, and dried at 80°C for 10 min. A 2:1000 (v/v) solution of fluorescent beads (FluoSpheres carboxylate–modified microspheres, 0.1 or 0.2 μm) in Millipore water is sonicated during 5 min and filtered using a 0.45-μm filter. Activated substrates are then incubated in the fluorescent beads solution for 10 min, washed three times with Millipore water, and dried at 80°C for 10 min. Samples can be stored at room temperature under dark conditions for up to 2 to 3 weeks. FluoroDish is then coated overnight with an adhesive [rat-tail collagen I (200 μg/ml) in PBS] or antiadhesive reagent (pLL(20)-g[3.5]-PEG(2) (0.1 mg/ml) diluted in Hepes buffer) solution under biofilm.

Cluster loading

Clusters are filtered on a 70-μm strainer (EASYStrainer, 542070), pelleted by a 400*g* pulse centrifugation and deposited on the two-dimensional PDMS substrate. Clusters on PEG substrate are overlaid with an agarose pad to prevent them from floating. They are then incubated overnight with culture medium in this configuration before imaging.

SDS treatment and imaging

Time-lapse imaging was done using a spinning disk confocal microscope Andor on DMI8, powered by Metamorph software. A first image of the sample is taken, and then, SDS (Sigma-Aldrich, L3771) is added with a syringe either directly on top of the clusters on collagen-I–coated FluoroDish or through the agarose pad on top of clusters on pLL-PEG–coated substrates. Sample is imaged every 1 min until the cell cluster is completely dissociated.

Plasmids, virus production, and infection

Plasmids

The DH-PH domain of ARHGEF11 was amplified and cloned into CRY2PHR-mCherry. pCIBN(deltaNLS)-pmGFP (Addgene plasmid no. 26867; http://n2t.net/addgene:26867; RRID: Addgene_26867) (*45*) and pCRY2PHR-mCherryN1 (Addgene plasmid no. 26866; http://n2t.net/addgene:26866; RRID: Addgene_26866) (*45*) are a gift from C. Tucker. The H2B-RFP plasmid is a gift from the Hall lab. pLV-Ftractin-mRuby3-p2A-mTurquoise-MLC-IRES-Blast is a gift from Meyer and colleagues (*46*) (Addgene plasmid no. 85146; http://n2t.net/addgene:85146; RRID: Addgene_85146); mCherry-Paxillin is a gift from the Vignjevic lab; and pLentiblast-Paxillin-mTurquoise is a gift from Debnath and colleagues (*47*) (Addgene plasmid no. 74206; http://n2t.net/addgene:74206; RRID: Addgene_74206).

Virus production and infection

Ectopic expression of fluorescent probes is achieved using lentiviruses. Lentiviruses are obtained by cotransfection of the plasmid of interest with the packaging vectors pMD2G (Addgene plasmid no.12259; http://n2t.net/addgene:12259; RRID: Addgene_12259) and pCMVdR8.74 (Addgene plasmid no. 8455; http://n2t.net/addgene:8455; RRID: Addgene_8455) into human embryonic kidney 293T cells with the transfection reagent JetPrime (Polyplus, 114-15). Lentivirus-containing supernatants are collected on days 2 and 3 following transfection, concentrated by ultracentrifugation (24000*g*, 2 hours), and stored at −80°C.

Infection is performed, as previously described (*13*). Briefly, HT29-MTX (1×10^6 cells) are exposed to lentiviruses in 500 μl of full DMEM containing protamine (16 μg/ml) overnight before being sorted by fluorescence-activated cell sorter to establish stable cell lines. Cell lines were then used for experiments as specified in the figures and legends. optoRhoA HT29-MTX cells express ARHGEF11-CRY2PHR-mCherry and CIBN-GFP, and control cells express CRY2PHR-mCherryN1 and CIBN-eGFP-CaaX.

Imaging, microscope acquisition, and optogenetic experiments

Time-lapse imaging

Time-lapse bright-field imaging is done using an Olympus inverted X83 microscope with a Hamamatsu camera or a Spinning Disk CSU-W1 (Yokogawa) with a Prime 95B sCMOC camera. The latter is also used for live fluorescence imaging.

Imaging of integrin αV internalization

Before injection in the microchannels, clusters are incubated in DMSO for control condition or with 10 μM cRGD for 30 min. Transferrin (Alexa Fluor 488-transferrin; 5 μg/ml; Invitrogen, T13342) is also added for all conditions to reveal the endosomal fraction. Clusters are then injected in PEG-coated microchannels in full media containing Transferrin and cRGD or DMSO and incubated overnight. Integrin αV and transferrin are then imaged using a Spinning Disk CSU-W1 microscope (Yokogawa) with a Prime 95B sCMOC camera.

Optogenetics

Clusters are incubated in the chips for at least 1 hour before imaging. Experiments are performed at 37°C in 5% CO_2 in a heating

chamber (Pecon, Meyer Instruments, Houston, TX) placed on an inverted microscope model no. IX71 equipped with a 60× objective with numerical aperture of 1.45 (Olympus, Melville, NY) and a camera ORCA-Flash4 (Hamamatsu, Japan). The microscope is controlled with the software Metamorph (Molecular Devices, Eugene, OR). Differential interference contrast imaging is performed with a far-red filter in the illumination path to avoid CRY2 activation. Optogenetic stimulations are performed every 2 to 2.5 or 5 min with a digital micromirror device (DMD) in epi-mode (DLP Light Crafter, Texas Instruments) illuminated with a SPECTRA Light Engine (Lumencor, Beaverton, OR) at 440 ± 10 nm. Total internal reflection fluorescence (TIRF) images are acquired using an azimuthal TIRF module (iLas2; Roper Scientific, Tucson, AZ). An automated tracking algorithm is designed in MATLAB with a feedback-loop routine to ensure that the optogenetic activation is maintained in the specific area of interest.

Immunofluorescence, antibodies, histology, and immunohistochemistry

Immunofluorescence

TSIP#1 in Fig. 1B was fixed in 4% paraformaldehyde (PFA) after 24 hours of incubation in collagen I. Cell clusters in fig. S1F were fixed in PFA 4% for 10 min and embedded in a collagen-I gel before immunofluorescence, as described previously (*13*). Images were acquired with a SpinningDisk CSU-W1 (Yokogawa) with a Zyla sCMOC camera driven by an Olympus X83.

Antibodies and dyes

Primary antibodies used were as follows: anti-integrin ß1 [P5D2; Developmental Studies Hybridoma Bank (DSHB), deposited by E. A. Wayner (DSHB Hybridoma Product); 1:500] and pMLC T18/S18 (anti-phospho MLC T18/S19; Cell Signaling Technology, 3674S; 1:100 or 1:200). Secondary antibodies used were as follows: anti-mouse–fluorescein isothiocyanate (Jackson ImmunoResearch, 711-545-152; 1:500) and anti-rabbit–Alexa Fluor 647 (Jackson ImmunoResearch, 715-605-152; 1:250 or 1:500). Dyes used were as follows: Alexa Fluor phalloidin rhodamine (Life Technologies, AF12415, 1:1000), Alexa Fluor phalloidin 488 (Life Technologies, A12379, 1:1000), and 4′,6-diamidino-2-phenylindole (DAPI).

Histology and immunohistochemistry

CRC (micropapillary histotype) primary tumors obtained after chirurgical resection are formalin-fixed and paraffin-embedded (FFPE) according to the routine protocols. Three-millimeter sections of FFPE samples are deparaffinized, unmasked (Ph8), and rehydrated before hematoxylin/eosin/saffron staining or immunohistochemistry.

Immunohistochemistry

Sections are immunostained with ezrin (BD Biosciences, 610603; 1:100) or CK20-specific mouse monoclonal antibody (clone Ks20.8, Dako, Glostrup, Denmark). Stainings are performed with Ventana BenchMark XT immunostainer (ventana Medical Systems, Tucson, AZ) using an UltraView DABv3 kit (Ventana). The chromogene is 3,3′-diaminobenzidine in all the stainings.

Image analysis

Naming

"Speed" is computed as the average of the absolute values of every instantaneous displacement. "Velocity" is oriented and describes the final true displacement of objects: It is computed as the displacement vector between two time points or, by extension, as the algebraic displacement along one direction (usually the x direction).

Analysis of cluster displacements from bright-field time-lapse sequences

For bright-field movies, displacement of clusters centroid is tracked every hour using the Manual Tracking plugin in Fiji (*48*). Clusters that are too small to be confined or dissociating during the experiment are ignored. Speed (micrometer per day) corresponds to the accumulated distance over 12 to 24 hours, extrapolated to 24 hours. Persistence is calculated as the ratio of Euclidean distance traveled by the cluster monitored every 1 hour for 1 day, over its total displacement. Maximum speed is calculated as the maximum instantaneous speed. Maximum consecutive migration duration is the longest period of continuous migration over 1 pixel (1.07 or 1.369 μm) per hour. These last three metrics are calculated for clusters migrating more than 25 μm per day.

Cell segmentation for cell tracking in optogenetic experiments

Movies are analyzed using custom-built routines in Fiji (*48*) and MATLAB (MathWorks, Natick, MA). ARHGEF11-CRY2-mCherry signal is used to segment clusters by applying a Gaussian filter and a threshold. Trajectories are then analyzed in MATLAB, taking the displacement of the center of each segmented cluster along the microchannel. The beginning of the activation is considered as time 0 and origin of the position for all the trajectories. Trajectories are sometimes flipped to put all the activation on the same side (left side of the cluster).

Analysis of Paxillin foci

Paxillin images are treated in Fiji with the Subtract background plugin, using a 2-pixel rolling ball. Threshold is then set to highlight and best separate all the foci. The area of each structure is collected using the Analyze Particles plugin in Fiji, considering particles of 10 infinite sizes. The proportion of area covered by Paxillin foci is obtained by normalizing the sum of Paxillin foci individual areas by the total area of the cluster.

ITGAV internalization

To determine the endosomal fraction, the Transferrin images are thresholded to best delineate endosomes. The thresholded image is then used to create a mask that is transferred to the ITGAV image. The amount of ITGAV is calculated by summing the "integrated intensity value" of each region of interest (ROI) from the Transferrin image. The ITGAV image is then thresholded to determine the total amount of ITGAV. We then calculate the ratio of ITGAV signal contained in the Transferrin mask over the total ITGAV signal.

Analysis of bead displacements in TFM experiments

Time-sequence images of fluorescent beads are aligned using the SIFT algorithm in Fiji (*49*). Bead displacements between first and last time points are then calculated using the cross-correlation PIV plugin in Fiji (*50*). The heatmap of bead displacements is coded in MATLAB. Maximum bead displacement is computed as the mean of 0.2% highest displacement amplitudes (mean over at least three displacement vectors) from the PIV result on the entire image field. Variation coefficient is computed as the ratio of SD of bead displacement amplitudes over their mean. It characterizes the dispersion of the distribution of bead displacements by the cluster: The higher it is, the more localized bead displacements are. Orientation of bead displacement vectors is computed as the average of $\cos(\theta) = (u \cdot v)/(||u|| \times ||v||)$ where u is the vector pointing from the cluster centroid (computed using ROI analysis in Fiji) to the coordinates of each bead, v is the bead displacement vector, and $||u||$ (resp. $||v||$) is the amplitude of u (resp. v) vector. Traction forces exerted by clusters on the beads lead to a $\cos(\theta) > 0$, whereas $\cos(\theta) < 0$ corresponds to

pushing forces. On PEG-coated substrates, small pushing forces can be detected, probably due to the light confinement by the agarose pad.

Analysis of MLC polarization

Direction of migration for each cluster is determined by tracking its movement for at least 2 hours before fluorescence imaging. Myosin and actin are imaged in a median section of the cluster using a spinning disk fluorescence microscope. For analyzing the intensity at the cortex, a 20-pixel Subtract background is performed before using a 15-pixel-wide line scan to delineate the cortex and measure myosin intensity signal in each half of the cluster. The intensity in each half is normalized to the perimeter of the line scan to calculate the rear to front ratio (raw integrated density over perimeter).

Myosin flow analyses

Myosin flows are analyzed from movies of median sections of HT29-MTX clusters stably expressing mTurquoise-MLC using a custom-built routine in Fiji (*48*) and MATLAB (MathWorks, Natick, MA). Images are acquired every 1 to 5 min during 20 min to 7.4 hours and the MLC channel is used to map actomyosin flow dynamics in clusters. Background contribution is removed using a custom-built macro in Fiji before PIV analysis. A bounding rectangle is adjusted to the cluster shape at every time point to obtain the cluster centroid positions. The Stramer lab (King's College London, UK) PIV package, developed in MATLAB (*51*), is used to extract maps of myosin flow velocity vectors from the median section of clusters. The size of objects to be tracked is 4 μm (50% wider than the cluster cortex), and the size of the analysis window is the value of the mean displacement of myosin between two consecutive frames (5 to 7 μm).

A MATLAB code was developed to display and exploit the PIV analysis. Mean PIV map of myosin flows of all clusters was obtained in two steps: (i) averaging over time the PIV maps of individual clusters, centered around a reference position; and (ii) averaging the time-averaged PIV maps over the clusters. This leads to a time-averaged mean PIV map, averaged over the whole population of clusters considered. Myosin flow kinetics are extracted at every time point from observation windows in contact with the channel walls (both clusters sides): These windows are 2 μm wide, and we chose for each cluster at what distance to the ends of the cluster (front and back) they start and finish, to avoid considering the curvature of the clusters that is not in contact with the channel walls (Fig. 5F). In the cluster reference frame, for each cluster i, the amplitude of the fluctuations of myosin speeds (along the x axis only, fluct_i) is calculated by subtracting the average velocity of myosin flows at the contact (averaged over space and time, $\overline{v_x}$) to the instantaneous velocity of myosin of each pixel n ($v_{x,n}(t)$), and taking the absolute value of this quantity. These fluctuations are then averaged over space and over time for each cluster

$$\mathrm{fluct}_i = \frac{1}{t_{\mathrm{tot}}}\sum_{t=1}^{t_{\mathrm{tot}}}\frac{1}{n_{\mathrm{tot}}(t)}\sum_{n=1}^{n_{\mathrm{tot}}(t)}\mathrm{abs}(v_{x,n}(t)-\overline{v_x})$$

Analysis of myosin flows in single cells

HT29-MTX single cells are tracked every 21 to 27 s during 7 to 37 min. For four cells expressing mTurquoise-MLC, several myosin particles (four to seven) are tracked manually as well in the lab reference frame every 21 or 27 s using the Manual Tracking plugin in Fiji. Before PIV analysis in the cell reference frame, images are realigned on the first image using the template matching plugin with the option of slices alignment, and background contribution is reduced with a custom-built macro in Fiji similar to the clusters. PIV analysis is then performed in MATLAB with the Stramer lab (King's College London, UK) PIV package (*51*).

Analysis of nuclei movements

Median sections are imaged every 2 to 30 min for 20 min to 11 hours. For mTurquoise-MLC–expressing HT29-MTX clusters, images of median sections of mTurquoise-expressing HT29-MTX clusters are previously inverted on Fiji to track nuclei where myosin is not expressed. Then, for all HT29-MTX clusters (expressing mTurquoise-MLC or H2B-RFP), automated tracking of nuclei is performed on Fiji with TrackMate plugin (*52*). Centroids of clusters are tracked as well with the Manual Tracking plugin. A custom-made R code was used for further analysis and graphical representations. Nuclei velocities are extracted at every time point from observation windows in contact with the channel walls (both clusters sides) that are a cell width wide (15 μm) and start and finish 12 μm away from each end of the clusters (front and back) to avoid considering cells not in contact with the channel walls. In the cluster reference frame, for each cluster i, the fluctuations of nuclei speeds (along the x axis, fluct_i) are calculated like the fluctuations of myosin flow speeds (see the "Myosin flow analyses" section), by subtracting the average velocity of lateral nuclei (averaged over nuclei and time, $\overline{v_x}$) to the instantaneous velocity of each nucleus n ($v_{x,n}(t)$), and taking the absolute value of this quantity. These fluctuations are then averaged over nuclei and over time for each cluster.

SUPPLEMENTARY MATERIALS

Supplementary material for this article is available at https://science.org/doi/10.1126/sciadv.abp8416

REFERENCES AND NOTES

1. K. M. Yamada, M. Sixt, Mechanisms of 3D cell migration. *Nat. Rev. Mol. Cell Biol.* **20**, 738–752 (2019).
2. A. W. Lambert, D. R. Pattabiraman, R. A. Weinberg, Emerging biological principles of metastasis. *Cell* **168**, 670–691 (2017).
3. D. L. Bodor, W. Pönisch, R. G. Endres, E. K. Paluch, Of cell shapes and motion: The physical basis of animal cell migration. *Dev. Cell* **52**, 550–562 (2020).
4. M. Innocenti, New insights into the formation and the function of lamellipodia and ruffles in mesenchymal cell migration. *Cell Adh. Migr.* **12**, 401–416 (2018).
5. E. K. Paluch, I. M. Aspalter, M. Sixt, Focal adhesion-independent cell migration. *Annu. Rev. Cell Dev. Biol.* **32**, 469–490 (2016).
6. Y.-J. Liu, M. Le Berre, F. Lautenschlaeger, P. Maiuri, A. Callan-Jones, M. Heuzé, T. Takaki, R. Voituriez, M. Piel, Confinement and low adhesion induce fast amoeboid migration of slow mesenchymal cells. *Cell* **160**, 659–672 (2015).
7. P. Friedl, J. Locker, E. Sahai, J. E. Segall, Classifying collective cancer cell invasion. *Nat. Cell Biol.* **14**, 777–783 (2012).
8. P. Friedl, D. Gilmour, Collective cell migration in morphogenesis, regeneration and cancer. *Nat. Rev. Mol. Cell Biol.* **10**, 445–457 (2009).
9. K. J. Cheung, A. J. Ewald, A collective route to metastasis: Seeding by tumor cell clusters. *Science* **352**, 167–169 (2016).
10. R. Mayor, S. Etienne-Manneville, The front and rear of collective cell migration. *Nat. Rev. Mol. Cell Biol.* **17**, 97–109 (2016).
11. E. Theveneau, C. Linker, Leaders in collective migration: Are front cells really endowed with a particular set of skills? *F1000Res* **6**, 1899 (2017).
12. A. Shellard, A. Szabó, X. Trepat, R. Mayor, Supracellular contraction at the rear of neural crest cell groups drives collective chemotaxis. *Science* **362**, 339–343 (2018).
13. O. Zajac, J. Raingeaud, F. Libanje, C. Lefebvre, D. Sabino, I. Martins, P. Roy, C. Benatar, C. Canet-Jourdan, P. Azorin, M. Polrot, P. Gonin, S. Benbarche, S. Souquere, G. Pierron, D. Nowak, L. Bigot, M. Ducreux, D. Malka, C. Lobry, J.-Y. Scoazec, C. Eveno, M. Pocard, J.-L. Perfettini, D. Elias, P. Dartigues, D. Goéré, F. Jaulin, Tumour spheres with inverted polarity drive the formation of peritoneal metastases in patients with hypermethylated colorectal carcinomas. *Nat. Cell Biol.* **20**, 296–306 (2018).
14. D. Krndija, F. El Marjou, B. Guirao, S. Richon, O. Leroy, Y. Bellaiche, E. Hannezo, D. Matic Vignjevic, Active cell migration is critical for steady-state epithelial turnover in the gut. *Science* **365**, 705–710 (2019).

15. B. Weigelin, G.-J. Bakker, P. Friedl, Intravital third harmonic generation microscopy of collective melanoma cell invasion: Principles of interface guidance and microvesicle dynamics. *Dermatol. Int.* **1**, 32–43 (2012).
16. A. Reversat, F. Gaertner, J. Merrin, J. Stopp, S. Tasciyan, J. Aguilera, I. de Vries, R. Hauschild, M. Hons, M. Piel, A. Callan-Jones, R. Voituriez, M. Sixt, Cellular locomotion using environmental topography. *Nature* **582**, 582–585 (2020).
17. T. Lämmermann, B. L. Bader, S. J. Monkley, T. Worbs, R. Wedlich-Söldner, K. Hirsch, M. Keller, R. Förster, D. R. Critchley, R. Fässler, M. Sixt, Rapid leukocyte migration by integrin-independent flowing and squeezing. *Nature* **453**, 51–55 (2008).
18. M. Bergert, A. Erzberger, R. A. Desai, I. M. Aspalter, A. C. Oates, G. Charras, G. Salbreux, E. K. Paluch, Force transmission during adhesion-independent migration. *Nat. Cell Biol.* **17**, 524–529 (2015).
19. C. Hidalgo-Carcedo, S. Hooper, S. I. Chaudhry, P. Williamson, K. Harrington, B. Leitinger, E. Sahai, Collective cell migration requires suppression of actomyosin at cell–cell contacts mediated by DDR1 and the cell polarity regulators Par3 and Par6. *Nat. Cell Biol.* **13**, 49–59 (2011).
20. D. Cai, S.-C. Chen, M. Prasad, L. He, X. Wang, V. Choesmel-Cadamuro, J. K. Sawyer, G. Danuser, D. J. Montell, Mechanical feedback through E-cadherin promotes direction sensing during collective cell migration. *Cell* **157**, 1146–1159 (2014).
21. C. D. Madsen, S. Hooper, M. Tozluoglu, A. Bruckbauer, G. Fletcher, J. T. Erler, P. A. Bates, B. Thompson, E. Sahai, STRIPAK components determine mode of cancer cell migration and metastasis. *Nat. Cell Biol.* **17**, 68–80 (2015).
22. L. Valon, A. Marín-Llauradó, T. Wyatt, G. Charras, X. Trepat, Optogenetic control of cellular forces and mechanotransduction. *Nat. Commun.* **8**, 14396 (2017).
23. V. Ruprecht, S. Wieser, A. Callan-Jones, M. Smutny, H. Morita, K. Sako, V. Barone, M. Ritsch-Marte, M. Sixt, R. Voituriez, C.-P. Heisenberg, Cortical contractility triggers a stochastic switch to fast amoeboid cell motility. *Cell* **160**, 673–685 (2015).
24. G. Beaune, C. Blanch-Mercader, S. Douezan, J. Dumond, D. Gonzalez-Rodriguez, D. Cuvelier, T. Ondarçuhu, P. Sens, S. Dufour, M. P. Murrell, F. Brochard-Wyart, Spontaneous migration of cellular aggregates from giant keratocytes to running spheroids. *Proc. Natl. Acad. Sci. U.S.A.* **115**, 12926–12931 (2018).
25. K. M. Stroka, H. Jiang, S.-H. Chen, Z. Tong, D. Wirtz, S. X. Sun, K. Konstantopoulos, Water permeation drives tumor cell migration in confined microenvironments. *Cell* **157**, 611–623 (2014).
26. A. Baule, K. V. Kumar, S. Ramaswamy, Exact solution of a Brownian inchworm model for self-propulsion. *J. Stat. Mech.* **2008**, P11008 (2008).
27. E. M. Purcell, Life at low Reynolds number. *Am. J. Phys.* **45**, 3–11 (1977).
28. A. Najafi, R. Golestanian, Simple swimmer at low Reynolds number: Three linked spheres. *Phys. Rev. E Stat. Nonlin. Soft Matter Phys.* **69**, 062901 (2004).
29. L. Giomi, N. Hawley-Weld, L. Mahadevan, Swarming, swirling and stasis in sequestered bristle-bots. *Proc. R. Soc. A Math. Phys. Eng. Sci.* **469**, 20120637 (2013).
30. A. Deblais, T. Barois, T. Guerin, P. H. Delville, R. Vaudaine, J. S. Lintuvuori, J. F. Boudet, J. C. Baret, H. Kellay, Boundaries control collective dynamics of inertial self-propelled robots. *Phys. Rev. Lett.* **120**, 188002 (2018).
31. Y. Wu, J. K. Yim, J. Liang, Z. Shao, M. Qi, J. Zhong, Z. Luo, X. Yan, M. Zhang, X. Wang, R. S. Fearing, R. J. Full, L. Lin, Insect-scale fast moving and ultrarobust soft robot. *Sci. Robot.* **4**, eaax1594 (2019).
32. S. Kriegman, D. Blackiston, M. Levin, J. Bongard, A scalable pipeline for designing reconfigurable organisms. *Proc. Natl. Acad. Sci. U.S.A.* **117**, 1853–1859 (2020).
33. P. Friedl, S. Alexander, Cancer invasion and the microenvironment: Plasticity and reciprocity. *Cell* **147**, 992–1009 (2011).
34. C. D. Paul, P. Mistriotis, K. Konstantopoulos, Cancer cell motility: Lessons from migration in confined spaces. *Nat. Rev. Cancer* **17**, 131–140 (2017).
35. D. J. Ruiter, J. H. van Krieken, G. N. van Muijen, R. M. de Waal, Tumour metastasis: Is tissue an issue? *Lancet Oncol.* **2**, 109–112 (2001).
36. S.-B. Lim, C. S. Yu, S. J. Jang, T. W. Kim, J. H. Kim, J. C. Kim, Prognostic significance of lymphovascular invasion in sporadic colorectal cancer. *Dis. Colon Rectum* **53**, 377–384 (2010).
37. V. Barresi, L. Reggiani Bonetti, E. Vitarelli, C. Di Gregorio, M. P. de Leon, G. Barresi, Immunohistochemical assessment of lymphovascular invasion in stage I colorectal carcinoma: Prognostic relevance and correlation with nodal micrometastases. *Am. J. Surg. Pathol.* **36**, 66–72 (2012).
38. M. Brown, F. P. Assen, A. Leithner, J. Abe, H. Schachner, G. Asfour, Z. Bago-Horvath, J. V. Stein, P. Uhrin, M. Sixt, D. Kerjaschki, Lymph node blood vessels provide exit routes for metastatic tumor cell dissemination in mice. *Science* **359**, 1408–1411 (2018).
39. J. Law, E. Martin, in *Concise Medical Dictionary* (Oxford Univ. Press, ed. 10, 2020).
40. S. J. Lord, K. B. Velle, R. D. Mullins, L. K. Fritz-Laylin, SuperPlots: Communicating reproducibility and variability in cell biology. *J. Cell Biol.* **219**, e202001064 (2020).
41. M. Fujii, M. Shimokawa, S. Date, A. Takano, M. Matano, K. Nanki, Y. Ohta, K. Toshimitsu, Y. Nakazato, K. Kawasaki, T. Uraoka, T. Watanabe, T. Kanai, T. Sato, A colorectal tumor organoid library demonstrates progressive loss of niche factor requirements during tumorigenesis. *Cell Stem Cell* **18**, 827–838 (2016).
42. S. Julien, A. Merino-Trigo, L. Lacroix, M. Pocard, D. Goéré, P. Mariani, S. Landron, L. Bigot, F. Nemati, P. Dartigues, L.-B. Weiswald, D. Lantuas, L. Morgand, E. Pham, P. Gonin, V. Dangles-Marie, B. Job, P. Dessen, A. Bruno, A. Pierré, H. De Thé, H. Soliman, M. Nunes, G. Lardier, L. Calvet, B. Demers, G. Prévost, P. Vrignaud, S. Roman-Roman, O. Duchamp, C. Berthet, Characterization of a large panel of patient-derived tumor xenografts representing the clinical heterogeneity of human colorectal cancer. *Clin. Cancer Res.* **18**, 5314–5328 (2012).
43. J. Drost, W. R. Karthaus, D. Gao, E. Driehuis, C. L. Sawyers, Y. Chen, H. Clevers, Organoid culture systems for prostate epithelial and cancer tissue. *Nat. Protoc.* **11**, 347–358 (2016).
44. F. Grillet, E. Bayet, O. Villeronce, L. Zappia, E. L. Lagerqvist, S. Lunke, E. Charafe-Jauffret, K. Pham, C. Molck, N. Rolland, J. F. Bourgaux, M. Prudhomme, C. Philippe, S. Bravo, J. C. Boyer, L. Canterel-Thouennon, G. R. Taylor, A. Hsu, J. M. Pascussi, F. Hollande, J. Pannequin, Circulating tumour cells from patients with colorectal cancer have cancer stem cell hallmarks in ex vivo culture. *Gut* **66**, 1802–1810 (2017).
45. M. J. Kennedy, R. M. Hughes, L. A. Peteya, J. W. Schwartz, M. D. Ehlers, C. L. Tucker, Rapid blue-light-mediated induction of protein interactions in living cells. *Nat. Methods* **7**, 973–975 (2010).
46. A. Hayer, L. Shao, M. Chung, L.-M. Joubert, H. W. Yang, F.-C. Tsai, A. Bisaria, E. Betzig, T. Meyer, Engulfed cadherin fingers are polarized junctional structures between collectively migrating endothelial cells. *Nat. Cell Biol.* **18**, 1311–1323 (2016).
47. C. M. Kenific, S. J. Stehbens, J. Goldsmith, A. M. Leidal, N. Faure, J. Ye, T. Wittmann, J. Debnath, NBR1 enables autophagy-dependent focal adhesion turnover. *J. Cell Biol.* **212**, 577–590 (2016).
48. J. Schindelin, I. Arganda-Carreras, E. Frise, V. Kaynig, M. Longair, T. Pietzsch, S. Preibisch, C. Rueden, S. Saalfeld, B. Schmid, J.-Y. Tinevez, D. J. White, V. Hartenstein, K. Eliceiri, P. Tomancak, A. Cardona, Fiji: An open-source platform for biological-image analysis. *Nat. Methods* **9**, 676–682 (2012).
49. D. G. Lowe, Distinctive image features from scale-invariant keypoints. *Int. J. Comput. Vis.* **60**, 91–110 (2004).
50. Q. Tseng, E. Duchemin-Pelletier, A. Deshiere, M. Balland, H. Guillou, O. Filhol, M. Théry, Spatial organization of the extracellular matrix regulates cell-cell junction positioning. *Proc. Natl. Acad. Sci. U.S.A.* **109**, 1506–1511 (2012).
51. L. Yolland, M. Burki, S. Marcotti, A. Luchici, F. N. Kenny, J. R. Davis, E. Serna-Morales, J. Müller, M. Sixt, A. Davidson, W. Wood, L. J. Schumacher, R. G. Endres, M. Miodownik, B. M. Stramer, Persistent and polarized global actin flow is essential for directionality during cell migration. *Nat. Cell Biol.* **21**, 1370–1381 (2019).
52. J.-Y. Tinevez, N. Perry, J. Schindelin, G. M. Hoopes, G. D. Reynolds, E. Laplantine, S. Y. Bednarek, S. L. Shorte, K. W. Eliceiri, TrackMate: An open and extensible platform for single-particle tracking. *Methods* **115**, 80–90 (2017).
53. K. V. Kumar, S. Ramaswamy, M. Rao, Active elastic dimers: Self-propulsion and current reversal on a featureless track. *Phys. Rev. E Stat. Nonlin. Soft Matter Phys.* **77**, 020102 (2008).
54. A. W. C. Lau, T. C. Lubensky, State-dependent diffusion: Thermodynamic consistency and its path integral formulation. *Phys. Rev. E Stat. Nonlin. Soft Matter Phys.* **76**, 011123 (2007).
55. L. F. Cugliandolo, V. Lecomte, F. van Wijland, Building a path-integral calculus: A covariant discretization approach. *J. Phys. A: Math. Theor.* **52**, 50LT01 (2019).
56. L. F. Cugliandolo, V. Lecomte, Rules of calculus in the path integral representation of white noise Langevin equations: The Onsager–Machlup approach. *J. Phys. A: Math. Theor.* **50**, 345001 (2017).
57. J. M. Sancho, M. S. Miguel, D. Dürr, Adiabatic elimination for systems of Brownian particles with nonconstant damping coefficients. *J. Stat. Phys.* **28**, 291–305 (1982).
58. R. F. Fox, Functional-calculus approach to stochastic differential equations. *Phys Rev A* **33**, 467–476 (1986).
59. E. A. Novikov, Functionals and the random-force method in turbulence theory. *Soviet J. Exp. Theor. Phys.* **20**, 1290–1294 (1965).
60. D. Ryter, Brownian motion in inhomogeneous media and with interacting particles. *Zeitschrift fur Physik B Condensed Matter.* **41**, 39–42 (1981).
61. D. Ryter, U. Deker, Properties of the noise-induced '"spurious"' drift. I. *J. Math. Phys.* **21**, 2662–2665 (1980).
62. U. Deker, D. Ryter, Properties of the noise-induced '"spurious"' drift. II. Simplifications of Langevin equations. *J. Math. Phys.* **21**, 2666–2669 (1980).
63. S. P. Das, R. Schilling, Fluctuating hydrodynamics and diffusion in amorphous solids. *Phys. Rev. E.* **50**, 1265–1273 (1994).
64. SMART. *Servier Medical Art*; https://smart.servier.com/.

Acknowledgments: We thank the patients for accepting to enroll in our study, the members of the Jaulin, Voituriez, Piel, and Montagnac laboratories and S. Ramaswamy for helpful discussions. We thank T. Manoliu and C. Laplace from the PFIC facility for technical help. We thank M. Polrot from the PFEP facility for assistance with the animal work. We thank C. Robert's lab for the plasma cleaner and cell lines. We thank G. Belthier, J. Pannequin lab, and F. André's lab for cell lines. We thank W. Beng and K. Vaidziulyte for the automated tracking algorithm

used in optogenetics. **Funding:** This work was supported by Agence Nationale de la Recherche (ANR) grant ANR-20-CE13-0031-01 (F.J., M.P., M.C., and R.V.), Institut National du Cancer (INCa) grants 2018-1-PLBIO-04-IGR-1 and 2020-1-PLBIO-04-IGR-1 (F.J. and M.P.), Fondation ARC grant PAJ20181208275 (F.J.), Ligue Nationale Contre le Cancer Île-de-France (LNCC-IDF) grant R19102LL (F.J.), Fundraising against CRC from the Gustave Roussy foundation (F.J.), ANR Laboratoires d'Excellence (LABEX) grant CelTisPhyBio ANR-10-LBX-0038 (M.C.), ANR Initiatives d'Excellence (IDEX) Paris Sciences et Lettres grant ANR-10-IDEX-0001-02 PSL (M.C.), ANR Institut Convergences Q-life grant ANR-17-CONV-0005 (M.C.), ANR (R.V.), Fondation pour la Recherche Médicale (FRM) (R.V. and E.D.), INCa (R.V.), Philanthropia fellowship (D.-L.P.), Taxe d'Apprentissage from Université Paris-Saclay grants 2019 and 2020 (D.-L.P.), and Ecole Polytechnique AMX fellowship (J.d.S.), with financial support from Inserm Cancer (F.J.) and CNRS (J.R.). **Author contributions:** Conceptualization: F.J., M.P., R.V., M.C., D.-L.P., E.D., J.d.S., E.G., and A. Mai. Formal analysis: D.-L.P., E.D., J.d.S., E.G., A. Mai., A. Mac., L.W., G.L., and R.L. Resources: D.-L.P., E.D., M.C., J.d.S., E.G., A. Mac., L.W., G.L., R.L., J.C., C.C.-J., J.R., M.D., M.G., and J.-Y.S. Software: D.-L.P., M.C., J.D.S., E.G., A. Mai., and G.L. Methodology: F.J., M.P., R.V., M.C., D.-L.P., E.D., J.d.S., E.G., A. Mai., L.W., and R.L. Investigation: D.-L.P., E.D., J.d.S., E.G., A. Mac., L.W., G.L., R.L., J.R., and M.L. Visualization: F.J., M.P., R.V., M.C., D.-L.P., E.D., J.d.S., E.G., and A. Mai. Funding acquisition: F.J., M.P., R.V., M.C., D.-L.P., E.D., and J.d.S. Project administration: F.J., D.-L.P., and E.D. Supervision: F.J., M.P., M.C., R.V., and E.D. Writing—original draft: F.J., M.P., R.V., M.C., D.-L.P., E.D., J.d.S., E.G., and A. Mai. Writing—review and editing: F.J., M.P., R.V., D.-L.P., E.D., E.G., and A. Mai. **Competing interests:** The authors declare that they have no competing interests. **Data and materials availability:** All data needed to evaluate the conclusions in the paper are present in the paper and/or the Supplementary Materials.

Submitted 1 March 2022
Accepted 3 August 2022
Published 30 September 2022
10.1126/sciadv.abp8416

ScienceAdvances

Cell clusters adopt a collective amoeboid mode of migration in confined nonadhesive environments

Diane-Laure PagèsEmmanuel DornierJean de SezeEmilie GontranAnanyo MaitraAurore MaciejewskiLi WangRui LuanJérôme CartryCharlotte Canet-JourdanJoël RaingeaudGrégoire LemahieuMarceline LebelMichel DucreuxMaximiliano GelliJean-Yves ScoazecMathieu CoppeyRaphaël VoituriezMatthieu PielFanny Jaulin

Sci. Adv., 8 (39), eabp8416. • DOI: 10.1126/sciadv.abp8416

Science Advances (ISSN) is published by the American Association for the Advancement of Science. 1200 New York Avenue NW, Washington, DC 20005. The title *Science Advances* is a registered trademark of AAAS.